tion recorded in this plane is given by

$$I(x',y')_{z'_0} = \iiint C'(m',n',r')T'(m',n',r')\, e^{i2\pi(m'x'+n'y'+r'z'_0)}\,\mathrm{d}m'\mathrm{d}n'\mathrm{d}r', \tag{3}$$

where z'_0 denotes the position of the oblique plane in the specimen and the co-ordinate system in Fourier space has been rotated so that $m' = m\cos\theta + r\sin\theta$, $n' = n$ and $r' = -m\sin\theta + r\cos\theta$. C' and T' therefore represent the OTF and object spatial frequency distributions in this rotated co-ordinate system. The spatial frequency content of the resulting oblique plane image can be found by taking the 2D Fourier transform of Eq. 3:

$$G(m'',n'') = \iint I(x',y')_{z'_0}\, e^{-i2\pi(m''x'+n''y')}\mathrm{d}x'\mathrm{d}y' \tag{4}$$

with new spatial frequency variables n'' and m''. Integration in x' and y' then leads to a simplification:

$$G(m'',n'') = \int C'(m'',n'',r')\,T'(m'',n'',r')\,e^{i2\pi r'z'_0}\,\mathrm{d}r'. \tag{5}$$

This is equivalent to a projection of the product of the object spatial frequency spectrum and the OTF for the system along the r' direction as defined in Fig. 1c, equal to $-m\sin(\theta) + r\cos(\theta)$. With this knowledge we can now, for any oblique plane, carry out such a projection of the three-dimensional region of support to find the possible spatial frequency components that may appear in the final image. It is clear on geometric grounds, that the cutoff frequency along the rotational axis of the plane, here the y-direction, is unaffected by the projection process. In contrast the cutoff, m''_1, along the x'-direction, diminishes with higher angles. Simple geometry provides us with an expression for this cutoff in terms of θ:

$$m''_1 = \begin{cases} \frac{4n\sin(\alpha)}{\lambda}\cos\theta, & 0 \le \tan\theta \le \frac{1}{2}\cot\left(\frac{\alpha}{2}\right), \\ \frac{n\cos^2(\alpha/2)}{\lambda}\left[2\tan\left(\frac{\alpha}{2}\right)+\cot\theta\right]^2\sin\theta, & \frac{1}{2}\cot\left(\frac{\alpha}{2}\right) < \tan\theta \le \tan\left(\frac{\pi}{2}\right). \end{cases} \tag{6}$$

This variation is plotted in Fig. 2 using solid lines for a 1.4 NA oil immersion lens and a 0.8 NA water dipping lens for θ in the range $(0, 90^\circ)$.

It is important to remind ourselves that the presence of a particular spatial frequency in a two-dimensional image gives no indication as to whether this represents a **k**-vector lying wholly within the plane or whether it is a projection of it into the plane. Although the value of the out-of-plane component cannot be known exactly it is limited to a range of values constrained by the 3D OTF region of support. For instance, in Fig. 1c all **k**-vectors shown in red have the same projection along the r'-axis so will appear in the oblique plane image with the same spatial frequency. Any other **k**-vector with the same projected value but lying outside the region of support will not appear in the final image.

An interesting consequence arises from this: in some cases a spatial frequency component can be present in an image that could not possibly have arisen from a **k**-vector lying wholly in the image plane. An example of this is shown in Fig. 1d. When imaging an oblique plane, spatial frequency $\mathbf{k}_1$, lying in the x-y plane, will appear in the final image with a projected magnitude, $|\mathbf{k}_1|\cos(\theta)$, whereas spatial frequency $\mathbf{k}_2$, that lies in the oblique plane and has the same length as the projection of $\mathbf{k}_1$, would not appear since it falls outside the 3D OTF region of support (shaded) and so cannot be imaged by the microscope. This point is further emphasized in Fig. 2 where we show as dashed lines the limiting values of in-plane spatial frequencies which may appear in the image along the x'-direction for planes oblique angles from 0° to 90°. Geometrically this cutoff, m''_2, is given by:

$$m''_2 = \begin{cases} \frac{4n\cos^2(\alpha/2)}{\lambda}\left(2\tan\left(\frac{\alpha}{2}\right)-\tan\theta\right)\sec\theta, & 0 \le \theta \le \frac{\alpha}{2}, \\ \frac{4n\sin^2(\alpha/2)}{\lambda}\,\mathrm{cosec}\,\theta, & \frac{\alpha}{2} < \theta \le \frac{\pi}{2}. \end{cases} \tag{7}$$

#134837 - $15.00 USD Received 8 Sep 2010; revised 25 Jan 2011; accepted 25 Jan 2011; published 27 Jan 2011

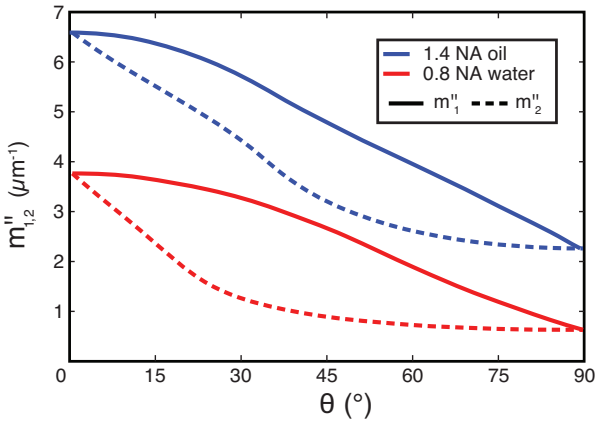

Fig. 2. Limiting values of spatial frequencies along the x'-direction for a 1.4 NA oil immersion objective and a 0.8 NA water immersion objective. Solid lines show the absolute spatial frequency cutoff which includes projections of out-of-plane spatial frequencies whereas dashed lines show the largest spatial frequencies that can be imaged of features lying wholly in the plane.

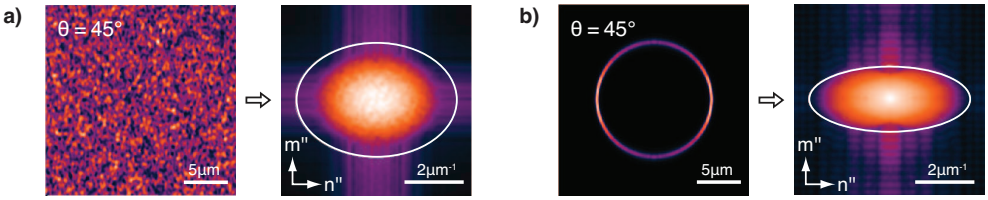

Fig. 3. Numerical simulations of images from a 45° oblique plane with a 1.15 NA water immersion objective and associated Fourier transforms. (a) White noise with a projection of the 3D OTF region of support overlain and (b) a spherical shell of diameter 12μm with the cut through the 3D OTF overlain.

As an example we note that for images taken on a 45° oblique plane with a 0.8 NA, water-immersion lens, spatial frequencies in the upper two thirds of the spectrum along the m''-axis could not have arisen from specimen variation wholly in the inclined plane.

3. Numerical simulation of oblique-plane imaging

To illustrate these effects theoretically we begin by considering a specimen comprising full-spectrum, white noise with a high spatial frequency content in all directions. When imaging an oblique plane through this specimen we would expect the spatial frequency content along the m''-direction to be particularly rich in Fourier content because of the large number of out-of-plane components which are projected onto the image plane. Fig. 3a shows a numerical simulation of the image that would be acquired from a 45° plane with a 1.15 NA, water-immersion objective with $\lambda = 850$ nm. Alongside is shown the Fourier spectrum of this image with the projection of the 3D OTF region of support onto this plane. The spatial frequency content of the image matches the projected region of support with the limit in x' that of Eq. 6, m''_1. The frequency content outside arises as a numerical artifact from the discrete Fourier transform used in the simulation.

In a second example we simulate a different specimen, that of a thin, spherical shell whose

#134837 - $15.00 USD Received 8 Sep 2010; revised 25 Jan 2011; accepted 25 Jan 2011; published 27 Jan 2011

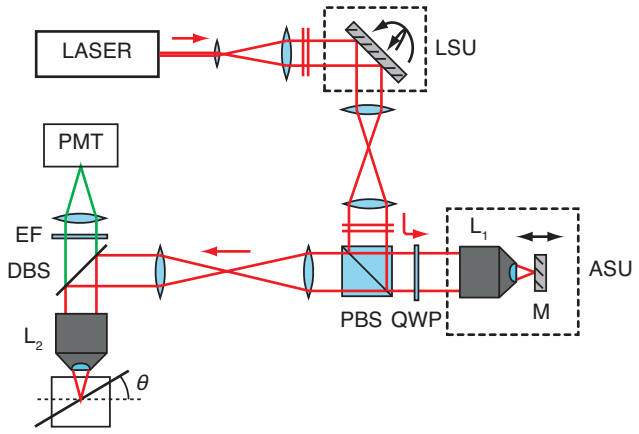

Fig. 4. Oblique plane scanning multi-photon microscope. The lateral scan unit (LSU) scans the focal spot laterally in the specimen and the axial scan unit (ASU) scans the spot axially. Oblique planes are scanned in three dimensions by using a combination of the LSU and ASU.

three-dimensional Fourier transform is known to vary with the form of a radial sinc function [9]. As the object spectrum extends broadly in all directions, this would initially suggest m_1'' angular variation as found with the noise simulation. However, the Fourier transform takes no account of the local distribution of spatial frequency content; the radial sinc function is built up from the Fourier integral over the entirety of the spherical shell and so oblique sections that do not contain the whole of the shell cannot contain the full spectrum. The **k**-vectors observed in the oblique plane image must therefore arise from the plane itself. The in-plane cutoff, m_2'', is then expected to dominate leading to a greater truncation of the observed spectrum. This is borne out by Fig. 3b where the m_2'' region of support determines the spatial frequency content in the image from a 45° plane through the simulated spherical shell. This is the effective support limit of the object-captured frequencies, and differs from that found in Fig.3a, where all regions of the OTF contribute to the final image.

4. Experimental verification of oblique-plane resolution phenomena

To confirm these observations experimentally we built the two-photon imaging system shown in Fig. 4. An axial scan unit [10] (ASU) was incorporated to scan the focal spot in the z-direction optically. The laser source used was a Ti:Sapphire laser (Tsunami, Spectra Physics), producing ultra-fast pulses with central wavelength 850 nm ($\Delta\lambda \sim 50$ nm, pulse length < 100 fs). Initially, this was expanded to form a plane wave with Gaussian width 5 mm and directed into the lateral scan unit (LSU), comprising two orthogonally mounted galvanometer mirrors (VM1000, Cambridge Technology, USA) that controlled the angular orientation of the wavefronts. From here the wavefronts were imaged into the pupil of L_1 in the ASU using a $4f$ imaging system comprising two achromatic doublet lenses, with focal lengths 120 mm and 160 mm, to produce a magnification of $4/3$. L_1 was an Olympus UApo/340, 40X, 0.9 NA dry objective, chosen for its favorable transmission characteristics at 850 nm. Light passing through L_1 was reflected off mirror M (PF03-03-P01, Thor labs) mounted on a flexible bridge assembly [10] between two galvanometers (VM1000+, Cambridge Technology, USA) for linear motion. The reflected light passed back through the lens and the emerging wavefront was then re-imaged into the pupil plane of L_2 using a further $4f$ system of achromatic doublets, this time with focal lengths 150 mm and 200 mm, to produce a magnification of $4/3$. It should be noted that the choice of

#134837 - $15.00 USD Received 8 Sep 2010; revised 25 Jan 2011; accepted 25 Jan 2011; published 27 Jan 2011

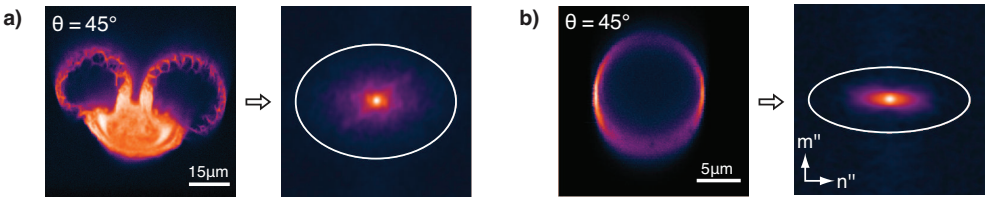

Fig. 5. Experimental images from a 45° oblique plane with a 1.15 NA water immersion objective and their associated Fourier transforms. (a) A fluorescent pollen grain with a projection of the OTF overlain and (b) a spherical shell with diameter 12μm with the cut through the OTF overlain.

this magnification is not trivial and for a full explanation of this parameter the reader is referred elsewhere [11]. All experiments were performed using an Olympus UApo/340, 40X, 1.15 NA water objective for L_2. A polarizing beam splitter (PBS) and quarter-wave plate (QWP) ensured all light entering the ASU was transmitted into the final stage of the system. A dichroic beamsplitter (DBS) and emission filter (EF) were used to separate fluorescence photons produced in the specimen in the range 400–720 nm for measurement on a digital PMT (P30PC-54, Sens-Tech). Photon counting and generation of galvanometer command voltage waveforms were performed through a reconfigurable I/O card with on-board FPGA (PCI-7830R, National instruments), operated from the Labview environment (National Instruments).

As an example of a specimen containing many spatial frequency components in all directions, a fluorescent pollen grain was selected for oblique plane imaging. Fig. 5a shows an image taken along a 45° plane together with the cutoff of Fig. 3a. The pollen grain contains, in this plane, frequency content in all directions leading to a fuller spectrum in the resulting image, with a region of support that is broadly matched in shape to the projection of the OTF along the r'-direction. The experiment was then repeated with a commercially available 12 μm spherical shell (F24634, Molecular probes, Invitrogen). For this case Fig. 5b shows in contrast the diminished spectrum arising from only the in-plane components, as observed in the numerical simulations.

In Fig. 5b it is observed that the deeper region of the imaged shell is more blurred than that nearer the surface. This is due to the microsphere being mounted in an optical cement with a refractive index of 1.52, in contrast to that of the immersion medium of the objective lens ($n = 1.33$). The step change in refractive index introduces increasing levels of spherical aberration when imaging deeper into the specimen, leading to the effect observed here. The spherical aberration can be incorporated into the simulation [12] or indeed corrected experimentally [13].

5. Conclusion

Increasingly researchers have found that, by tailoring scan geometries to a specific imaging problem, it is possible to acquire images from only the regions of interest in a specimen with much-improved temporal resolution compared with the acquisition and post-processing of a three-dimensional image stack. In this paper we have explored the ensuing limitation in resolution of such images by considering a plane inclined within a specimen volume. Our analysis, based on a consideration of the three-dimensional optical transfer function, has shown that the resolution becomes increasingly anisotropic with increasing angle of obliquity. We further showed that the inclined-plane images may contain spatial frequencies that cannot possibly have arisen wholly from in-plane spatial variations. For some configurations the maximum spatial frequency observed can be three times higher than the in-plane maximum. It is important therefore to exercise caution when analyzing images with the intent of extracting measurements

#134837 - $15.00 USD Received 8 Sep 2010; revised 25 Jan 2011; accepted 25 Jan 2011; published 27 Jan 2011

of periodic variations in a particular plane [14]. A corollary to this is that if the exact in-plane spatial variation is sought, post-processing with a digital filter derived from Eq. 7 would remove the misleading, higher-frequency modes. Likewise, we can take advantage of these supplementary modes when applying deconvolution techniques to the images.

While we have confined our analysis to inclined planes we note that, by taking a piecewise approach to the analysis, these conclusions are generalizable to all out-of-plane scan geometries, such as lines and curved surfaces.

Acknowledgements

CWS was funded by the Wellcome Trust. EJB held an EPSRC postdoctoral research fellowship (EP/F042647/1).

#134837 - $15.00 USD Received 8 Sep 2010; revised 25 Jan 2011; accepted 25 Jan 2011; published 27 Jan 2011